Research Article

Distinguishing Features of Longitudinal Magnetoconductivity for a Rarita-Schwinger-Weyl Node

Ipsita Mandal[1]

1. Department of Physics, Shiv Nadar Institution of Eminence (SNIoE), India

The band-degeneracy points in the Brillouin zones of chiral crystals exist in multiple avatars, with the high-symmetry points being able to host multifold nodes of distinct characters. A class of such crystals, assisted by the spin-orbit coupling, harbours fourfold degeneracy in the form of Rarita-Schwinger-Weyl node (RSWN) at the Γ-point. Our aim is to explore the nature of longitudinal magnetoconductivity, arising from applying collinear electric and magnetic fields, for such systems. Adjusting the chemical potential to lie near the intrinsic energy-location of the RSWN, the multifold nature of the RSWN is revealed by an interplay of intraband and interband scatterings, which would not arise in twofold degeneracies like the conventional Weyl nodes. The current study fills up the much-needed gap in obtaining the linear response from an exact computation, rather than the insufficient relaxation-time approximation employed earlier.

Correspondence: papers@team.qeios.com — Qeios will forward to the authors

I. Introduction

The unprecedented advancement on the experimental fronts, coupled with the DFT studies of materials, have put forward numerous generalisations of the archetypal Weyl semimetal (WSM) of the three-dimensional (3d) variety[1][2][3]. The excitement surrounding these so-called semimetallic systems mainly stems form the fact that their Brillouin zones (BZs) harbour nodal points, which, in turn, furnish the momentum space with the mathematical properties of topology[4][5][6][7], when viewed as closed manifolds. Physical properties like the Berry curvature (BC) and the orbital magnetic moment (OMM) quantify the topological properties lurking beneath, which are detectable in transport experiments[8][9][10][11][12][13][14][15][16][17][18]. Generalising the simplest prototype of an isotropic and linear-in-momentum twofold band-crossing, a pseudospin-3/2 Rarita-Schwinger-Weyl node (RWSN) [19][20][21][22][23][24][25][26][27][28][29][30] represents a fourfold band-crossing at a high-symmetry point of the BZ of a chiral crystal[19][31][32]. Adding to the cornucopia of transport properties that can reflect the exquisite character of RSWNs[15][26][28][29][30][33][34], we investigate here the longitudinal magnetoconductivity arising from an isolated node[35].

 doi.org/10.32388/NoMLRZ

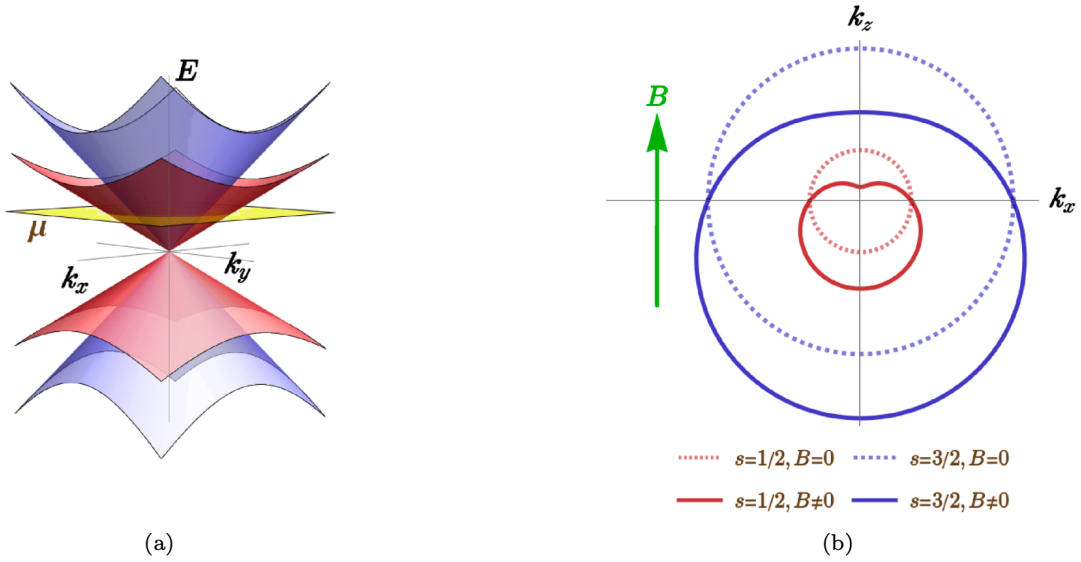

Figure 1. Schematics of the energy bands meeting at an isotropic RSWN: (a) Bare dispersion (E) for $s = \pm 1/2$ (light red) and $s = \pm 3/2$ (light blue) bands against the $k_x k_y$-plane (or, equivalently, $k_y k_z$- and $k_z k_x$-planes). The yellow plane depicts a positive chemical potential (μ) cutting the $s = 1/2$ and $s = 3/2$ bands, giving rise to two concentric Fermi surfaces. (b) Fermi-surface projections in the the $k_x k_y$-plane, when $\boldsymbol{B}$ (green arrow) is applied along the z-axis. To provide an eye-estimate, the dotted curves show the unperturbed projections in the absence of an external magnetic field.

The perks of invoking the analogy of the BC (existing in the momentum space) to a magnetic field (existing in the momentum space) is that we conjure up the intuitive picture of nonzero BC monopoles sitting at the nodal points[36][37], acting as the sources and sinks of the vector field of the BC-flux. Utilising the mathematical machinery of algebraic topology, the monopoles' charges also represent the so-called Chern numbers about the nodal points. The sign of $\mathcal{C}$ is pictured as the chirality (χ) of the node, conferring a notion of *handedness or chirality* on the quasiparticles populating the bands converging there. Appropriately, they are termed as *right-handed* or *left-handed* quasipartcles, depending on whether $\chi = 1$ or $\chi = -1$.

The appearance of chirally-charged nodes in 3d crystal-lattices is governed by the Nielsen-Ninomiya theorem[38], which is physically reflected by the fact that the sum of the Chern numbers over the entire BZ must yield zero. For nodes arising in achiral crystals (e.g., TaAs family[39]), such conjugate partners are typically (almost) degenerate in energy, due to the presence of mirror or other roto-inversion symmetries. Therein, charge-pumping is an important internode phenomenon in the presence of collinear external electric ($\boldsymbol{E}$) and magnetic ($\boldsymbol{B}$) fields. The phenomenon in question is an embodiment of the chiral anomaly in the arena of condensed matter physics[14][34][40][41], where the analog of the well-known concept of spacetime chirality (of relativistic fermions) is realised in the momentum space. It provides a sharp contrast with the oppositely-charged chiral nodes in chiral crystals, where they need not be degenerate in energy, because the conjugate nodes are not related by crystal symmetries. In fact, they are observed to have discernible separations in energy and momenta, with a isolated nodes sitting at their intrinsic chemical potentials[31][42][43]. The inevitable outcome is that the internode-scattering induced charge pumping gets irrelevant. However, at the same time, the energy-offset between the nodes of opposite chiralities fulfills the requisite

conditions for observing other important phenomena like quantised circular photogalvanic effect[19][31][44][45][46][47][48] and circular dichroism[26][49].

In our recent works, we have addressed the pertinent problem of computing longitudinal magnetoconductivity in systems where multiple bands contribute to transport at a particular node, encompassing the cases of chirally-conjugate nodes[17] and isolated Kramers-Weyl nodes[35] (the latter arising exclusively in chiral crystals[50][51]). In this paper, we take up a similar problem where an isotropic RSWN (sitting at the Γ-point) is the system under consideration. As pointed out earlier, only the isolated RWSN will be relevant here for computing the linear response, since we will consider tuning the external chemical potential to lie near the intrinsic energy of the concerned nodal point, safely assuming that the chirally-conjugate node is sufficiently separated in energy and momenta. For example, in RhSi, there exist fourfold- and sixfold-degenrate nodes at the Γ- and R-points of the BZ, carrying Chern numbers of ± 4, and featuring the largest possible momentum-separation between the nodal-points' locations[43][52]. While the former represents an RSWN, the bands at the latter are doubly-degenerate, featuring a pair of pseudospin-1 triple-point fermions (TPFs). The energy-offset between these nodes is ~ 0.4 eV. All these make it possible to observe really long Fermi arcs, spanning the distance constrained by the separation of the multiply-degenerate bulk-nodes, and topologically protected by their bulk chiral charges. Other examples of chiral crystals include AlPt[53], RhGe (with the energy-separatation between RSWN and the TPFs being ~ 0.21 eV)[54], sanchez[52] Li_2Pd_3B[55], Li_2Pt_3B[55], and CoSi[24][52].

A typical RSWN is depicted schematically in Fig. 1, with the four bands visualised near the degeneracy point. Exploiting the universal applicability of the Boltzmann equations as the kinetic theory for transport[56][57], we will carry out the exercise of computing the longitudinal conductivity exactly, arising from applying collinear electromagnetic fields ($\boldsymbol{E} \parallel \boldsymbol{B}$). The framework will be limited to the realm of weak (implying nonquantising) magnetic fields, so that the splitting of the dispersion into discrete Landau-levels can be ignored. Improving on our earlier ventures along similar lines [33][34], we will go beyond the relaxation-time approximation, thereby solving the semimeclassical Boltzmann equations exactly. To elaborate on the context further, we would like to point out that the nature of in-plane and out-of-plane components of conductivity in planar-Hall set-ups have been derived in Refs. [33][34], within the simplifying framework of the relaxation-time approximation, considered the aspects of intranode[33] and internode[34] scatterings. The current calculations will help us fix the shortcomings arising from the assumption of a momentum-independent relaxation-time.

The paper is organised as follows: In Sec. 2, we describe the explicit form of the low-energy effective Hamiltonian in the vicinity of an RSWN node, and the emerging topological properties. Sec. 3 is devoted to deriving the equations leading to the final values of the longitudinal magnetoconductivity. The results are discussed in Sec. 3.3 therein, illustrated by representative plots. Finally, we end with a summary and some future perspectives in Sec. 4. In all our expressions, we will adopt the natural units, which involves setting the reduced Planck's constant ($\hbar$), the speed of light (c), and the Boltzmann constant (k_B) to unity. Additionally, the electric charge has no units. Despite the fact that the magnitude (e) of a single unit of electrons' charge is unity, we will retain it in our expressions solely for the purpose of book-keeping.

II. Model

The widely used method of linearising the $\boldsymbol{k} \cdot \boldsymbol{p}$ Hamiltonian about a fourfold degeneracy at the Γ-point of a chiral crystal leads us to the generic forms of the RWSN nodes[43][58]. Adopting the isotropic version for the sake of simplicity, we use the model Hamiltonian captured by

$$\mathcal{H}(\boldsymbol{k}) = v_F\,(k_x\,\mathcal{J}_x + k_y\,\mathcal{J}_y + k_z\,\mathcal{J}_z)\,, \tag{1}$$

where $\boldsymbol{\mathcal{J}} = \{\mathcal{J}_x,\,\mathcal{J}_y,\,\mathcal{J}_z\}$ represents the vector operator whose three components comprise the the angular momentum operators in the spin-$3/2$ representation of the SU(2) group. We choose the commonly-used representation with

$$\mathcal{J}_x = \begin{pmatrix} 0 & \frac{\sqrt{3}}{2} & 0 & 0 \\ \frac{\sqrt{3}}{2} & 0 & 1 & 0 \\ 0 & 1 & 0 & \frac{\sqrt{3}}{2} \\ 0 & 0 & \frac{\sqrt{3}}{2} & 0 \end{pmatrix}, \quad \mathcal{J}_y = \begin{pmatrix} 0 & \frac{-i\sqrt{3}}{2} & 0 & 0 \\ \frac{i\sqrt{3}}{2} & 0 & -i & 0 \\ 0 & i & 0 & \frac{-i\sqrt{3}}{2} \\ 0 & 0 & \frac{i\sqrt{3}}{2} & 0 \end{pmatrix}, \quad \mathcal{J}_z = \begin{pmatrix} \frac{3}{2} & 0 & 0 & 0 \\ 0 & \frac{1}{2} & 0 & 0 \\ 0 & 0 & -\frac{1}{2} & 0 \\ 0 & 0 & 0 & -\frac{3}{2} \end{pmatrix}. \tag{2}$$

The energy eigenvalues are found to be

$$\varepsilon_s(k) = s\,v_F\,k\,, \quad s \in \left\{\pm\frac{1}{2}, \pm\frac{3}{2}\right\}, \tag{3}$$

where $k = \sqrt{k_x^2 + k_y^2 + k_z^2}$. Thus, each of the four bands demonstrates an isotropic linear-in-momentum dispersion like a Weyl cone [cf. Fig. 1(a)]. The signs of "$+$" and "$-$" give us the dispersion relations for the conduction and valence bands, respectively, with respect to the nodal point. The corresponding group velocities of the quasiparticles are given by

$$\boldsymbol{v}_s(\boldsymbol{k}) = \nabla_{\boldsymbol{k}}\varepsilon_s(\boldsymbol{k}) = \frac{s\,v_F\,\boldsymbol{k}}{k}\,. \tag{4}$$

The isotropy of $\mathcal{H}$ dictates that the simplicity of the spherical-polar coordinates can be employed by using the transformations of

$$k_x = k\sin\theta\cos\phi\,, \quad k_y = k\sin\theta\sin\phi\,, \quad k_z = k\cos\theta\,, \tag{5}$$

where $k \in [0, \infty)$, $\phi \in [0, 2\pi)$, and $\theta \in [0, \pi]$.

A. Eigenvectors

For an orthonormal set of eigenvectors, $\{\psi_s(\boldsymbol{k})\}$, the explicit forms of the positive-energy bands are given by

$$\begin{aligned} \psi_{1/2}(\boldsymbol{k}) &= \left[-\frac{\sqrt{3}\,e^{-3\,i\,\phi}\,(1-\cos^2\theta)\,\csc\left(\frac{\theta}{2}\right)}{4} \quad \frac{e^{-2\,i\,\phi}\,\cos\left(\frac{\theta}{2}\right)(3\cos\theta - 1)}{2} \quad \frac{e^{-i\,\phi}\sin\left(\frac{\theta}{2}\right)(3\cos\theta + 1)}{2} \quad \frac{\sqrt{3}\,\sin\left(\frac{\theta}{2}\right)\sin\theta}{2}\right]^{\mathrm{T}} \\ \text{and } \psi_{3/2}(\boldsymbol{k}) &= \left[e^{-3\,i\,\phi}\,\cos^3\left(\frac{\theta}{2}\right) \quad \frac{\sqrt{3}\,e^{-2\,i\,\phi}\,\sin^2\theta\,\csc\left(\frac{\theta}{2}\right)}{4} \quad \frac{\sqrt{3}\,e^{-i\,\phi}\sin\left(\frac{\theta}{2}\right)\sin\theta}{2} \quad \sin^3\left(\frac{\theta}{2}\right)\right]^{\mathrm{T}}. \end{aligned} \tag{6}$$

This will be used to determine the strength of the scattering cross-sections and, also, an ansatz for the nonequilibirum quasiparticle-distributions.

B. Topological quantities

Due to a nontrivial topology of the bandstructure, we need to compute the BC and the OMM, using the starting expressions of[5] [59]

$$\boldsymbol{\Omega}_s(\boldsymbol{k}) = i[\nabla_{\boldsymbol{k}}\psi_s(\boldsymbol{k})]^\dagger \times [\nabla_{\boldsymbol{k}}\psi_s(\boldsymbol{k})] \text{ and } \boldsymbol{m}^s(\boldsymbol{k}) = \frac{-\,i\,e}{2}\,[\nabla_{\boldsymbol{k}}\psi_s(\boldsymbol{k})]^\dagger \times \Big[\{\mathcal{H}(\boldsymbol{k}) - \varepsilon^s(\boldsymbol{k})\}\,\{\boldsymbol{\nabla}_{\boldsymbol{k}}\psi_s(\boldsymbol{k})\}\Big], \tag{7}$$

respectively. Evaluating these expressions for the RSW node described by $\mathcal{H}(\boldsymbol{k})$, we get[33][60]

$$\boldsymbol{\Omega}_s(\boldsymbol{k}) = \frac{-\,s\,\boldsymbol{k}}{k^3} \text{ and } \boldsymbol{m}_s(\boldsymbol{k}) = \frac{-\,e\,v_F\,\mathcal{G}_s\,\boldsymbol{k}}{k^2}\,, \text{ where } \{\mathcal{G}_{\pm1/2},\,\mathcal{G}_{\pm3/2}\} = \left\{\frac{7}{4},\,\frac{3}{4}\right\}. \tag{8}$$

Since $\boldsymbol{\Omega}_s(\boldsymbol{k})$ and $\boldsymbol{m}_s(\boldsymbol{k})$ are the intrinsic properties of the bandstructure, they depend only on the wavefunctions.

A nonzero BC manifests itself primarily via modifying the phase-space volume element, incorporated through the factor of[6][15][33][56][57][61]

$$\mathcal{D}_s(\boldsymbol{k}) = \left[1 + e\,\{\boldsymbol{B}\cdot\boldsymbol{\Omega}_s(\boldsymbol{k})\}\right]^{-1}. \tag{9}$$

This, in turn, it affects the explicit forms of the Hamilton's equations, which we will discuss In Sec. 3. On the other hand, the OMM distorts the Fermi surfaces along the direction of $\boldsymbol{B}$, by adding the term

$$\varepsilon_s^{(m)}(\boldsymbol{k}) = -\,\boldsymbol{B}\cdot\boldsymbol{m}_s(\boldsymbol{k})\,, \tag{10}$$

as schematically depicted in Fig. 1(b). Consequently, in addition to affecting the Fermi-Dirac distributions functions, it causes modifications of the group-velocities via adding

$$\boldsymbol{v}_s^{(m)}(\boldsymbol{k}) \equiv \nabla_{\boldsymbol{k}}\varepsilon_{(\sigma)}(\boldsymbol{k}) \tag{11}$$

to $\boldsymbol{v}_s(\boldsymbol{k})$.

III. Conductivity

In this section, we will review the step-by-step procedure to compute the electric conductivity, applying the machinery of semiclassical Boltzmann equations[6][12][15][17][33][56][57][61]. Although this has been demonstrated multiple times in our earlier works[17][35], it is primarily needed here to set the notations. The main line of arguments for obtaining the final equations was developed in Ref. [12], which we adapt and generalise for our system under study.

A. Kinetic equations driven by electromagnetic fields

The equilibrium Fermi-Dirac distribution,

$$f_0\big(\xi_s(\boldsymbol{k}),\mu,T\big) = \left[1+\exp\{(\xi_s(\boldsymbol{k})-\mu)/T\}\right]^{-1}, \tag{12}$$

where T is the temperature, contains the effective energy,

$$\xi_s(\boldsymbol{k}) = \varepsilon_s(\boldsymbol{k}) + \varepsilon_s^{(m)}(\boldsymbol{k})\,. \tag{13}$$

While using f_0 in various equations, we will be suppressing its μ- and T-dependence for uncluttering of notations. Furthermore, in what follows, we will perform our calculations by setting $T=0$.

The Hamilton's equations of motion for the electronic quasiparticles, occupying a given Bloch band, are described by[6][15][33][56][57][61]

$$\begin{aligned}
&\dot{\boldsymbol{r}} = \nabla_{\boldsymbol{k}}\,\xi_s - \dot{\boldsymbol{k}}\times\boldsymbol{\Omega}_s(\boldsymbol{k}) \text{ and } \dot{\boldsymbol{k}} = -\,e\,(\boldsymbol{E}+\dot{\boldsymbol{r}}\times\boldsymbol{B})\\
\Rightarrow\;&\dot{\boldsymbol{r}} = \mathcal{D}_s(\boldsymbol{k})\left[\boldsymbol{w}_s(\boldsymbol{k}) + e\,\boldsymbol{E}\times\boldsymbol{\Omega}_s(\boldsymbol{k}) + e\,\{\boldsymbol{\Omega}_s\cdot\boldsymbol{w}_s(\boldsymbol{k})\}\,\boldsymbol{B}\right] \text{ and } \dot{\boldsymbol{k}} = -\,e\,\mathcal{D}_s(\boldsymbol{k})\left[\boldsymbol{E}+\boldsymbol{w}_s(\boldsymbol{k})\times\boldsymbol{B} + e\,(\boldsymbol{E}\cdot\boldsymbol{B})\,\boldsymbol{\Omega}_s(\boldsymbol{k})\right],
\end{aligned} \tag{14}$$

where

$$\boldsymbol{w}_s(\boldsymbol{k}) = \boldsymbol{v}_s(\boldsymbol{k}) + \boldsymbol{v}_s^{(m)}(\boldsymbol{k})\,. \tag{15}$$

They reflect the nontrivial role played by a nonzero BC, as compared to the scenarios when the BC vanishes (see, for example, the systems discussed in Refs. [62][63]). In particular, an extra term in the form of $-\dot{\boldsymbol{k}}\times\boldsymbol{\Omega}_s$ represents an anomalous velocity, with the BC playing the counterpart of the magnetic field, albeit in the momentum space.

The bare-bones kinetic equation, arising out of the fundamental Boltzmann's transport formalism, is expressed as

$$[\partial_t + \boldsymbol{w}_s(\boldsymbol{k})\cdot\nabla_{\boldsymbol{r}} - e\,\{\boldsymbol{E}+\boldsymbol{w}_s(\boldsymbol{k})\times\boldsymbol{B}\}\cdot\nabla_{\boldsymbol{k}}]\, f_s(\boldsymbol{r},\boldsymbol{k},t) = I_{\rm coll}[f_s(\boldsymbol{k})]\,, \tag{16}$$

where $f_s(\boldsymbol{r},\boldsymbol{k},t)$ represents the nonequilibrium quasipaticle-distribution function associated with the band s. A slight deviation from $f_0(\xi_s(\boldsymbol{k}))$ is parametrised by $\delta f_s(\boldsymbol{r},\boldsymbol{k},t) \equiv f_s(\boldsymbol{r},\boldsymbol{k},t) - f_0(\xi_s(\boldsymbol{k}))$, caused by the the probe electric field, and is assumed to be of the same order of smallness as $|\boldsymbol{E}|$ (say, $\delta\varsigma$). Here, we restrict ourselves to spatially-uniform and time-independent electromagnetic fields. Consequently, f_s must must also be independent of position and time, so that $\delta f_s(\boldsymbol{r},\boldsymbol{k},t) = \delta f_s(\boldsymbol{k})$. When we retain terms upto linear-order-in-$\delta\varsigma$, we restrict ourselves to the so-called linear-response regime. The *collision integral*, $I_{\rm coll}[f_s(\boldsymbol{k})]$, takes care of the relevant scattering processes instrumental in relaxing $f_s(\boldsymbol{k})$ towards the equilibrium value of $f_0(\xi_s(\boldsymbol{k}))$.

For elastic point-scattering mechanisms, the collision integral takes the form of

$$I_{\rm coll}[f_s(\boldsymbol{k})] = \sum_{\tilde{s}}\int_{k'} \mathcal{M}_{s,\tilde{s}}(\boldsymbol{k},\boldsymbol{k}')\,[f_{\tilde{s}}(\boldsymbol{k}')) - f_s(\boldsymbol{k})]\,,\ \text{where}\ \int_k \equiv \int \frac{d^3\boldsymbol{k}}{(2\,\pi)^3\,\mathcal{D}_{\tilde{s}}(\boldsymbol{k}')} \tag{17}$$

symbolises the 3d momentum-space integral, incorporating the modified phase-space factor due to the BC. The scattering rate, not involving any energy-dissipation, is a direct consequence of the Fermi's golden rule, reflected by

$$\mathcal{M}_{s,\tilde{s}}(\boldsymbol{k},\boldsymbol{k}') = \frac{2\,\pi\,\rho_{\rm imp}}{V}\left|\{\psi_{\tilde{s}}(\boldsymbol{k}')\}^\dagger\,\mathcal{V}_{s,\tilde{s}}(\boldsymbol{k},\boldsymbol{k}')\,\psi_s(\boldsymbol{k})\right|^2\delta\Big(\xi_{\tilde{s}}(\boldsymbol{k}') - \xi_s(\boldsymbol{k})\Big)\,, \tag{18}$$

Here, $\rho_{\rm imp}$ embodies the impurity-concentration (acting as the scattering centres), V denotes the system's spatial volume, and $\mathcal{V}_{s,\tilde{s}}(\boldsymbol{k},\boldsymbol{k}')$ represents the scattering-potential matrix. Restricting to elastic and spinless scatters, $\mathcal{V}_{s,\tilde{s}}(\boldsymbol{k},\boldsymbol{k}') = \mathbb{I}_{2\times2}\,\mathcal{V}_{s,\tilde{s}}$, reducing to an identity matrix in the spinor space sans any momentum dependence. Thus, finally we can use the equation,

$$\mathcal{M}_{s,\tilde{s}}(\boldsymbol{k},\boldsymbol{k}') = \frac{2\,\pi\,\rho_{\rm imp}\,|\mathcal{V}_{s,\tilde{s}}|^2}{V}\left|\{\psi_{\tilde{s}}(\boldsymbol{k}')\}^\dagger\,\psi_s(\boldsymbol{k})\right|^2\delta\Big(\xi_{\tilde{\chi},\tilde{s}}(\boldsymbol{k}') - \xi_{\chi,s}(\boldsymbol{k})\Big)\,, \tag{19}$$

assisted by Eq. (6). Assuming a symmetric interband-scattering between the $s=1/2$ and $s=3/2$ bands, we parametrise the scattering strengths via two paremeters, expressed as

$$|\mathcal{V}_{1/2,1/2}|^2 \equiv \frac{16\times2\,\pi}{\rho_{\rm imp}}\,\beta^{1/2,1/2}_{\rm intra}\,,\quad |\mathcal{V}_{3/2,3/2}|^2 \equiv \frac{16\times2\,\pi}{\rho_{\rm imp}}\,\beta^{3/2,3/2}_{\rm intra}\,,\ \text{and}\ |\mathcal{V}_{s,\tilde{s}}|^2\big|_{s\neq\tilde{s}} \equiv \frac{16\times2\,\pi}{\rho_{\rm imp}}\,\beta_{\rm inter}\,. \tag{20}$$

Here, the subscripts "intra" and "inter" indicate the strengths of intraband and interband scatterings, respectively. In what follows, we will assume a pocitive chemical potential, $\mu>0$, being applied to the node, so that the bands with $s=1/2$ and $s=3/2$ contribute to transport at $T\to0$.

B. Linearised Boltzmann equation and its solutions

Gathering all the ingredients of the preceding subsections, we are now ready to solve the *linearised Boltzmann equation*, embodied by

$$-\,e\,\mathcal{D}_s(\boldsymbol{k})\left[\Big\{\boldsymbol{w}_s(\boldsymbol{k}) + e\,\Big(\boldsymbol{\Omega}_s(\boldsymbol{k})\cdot\boldsymbol{w}_s(\boldsymbol{k})\Big)\boldsymbol{B}\Big\}\cdot\boldsymbol{E}\ \ \frac{\partial f_0(\xi_s(\boldsymbol{k}))}{\partial\xi_s(\boldsymbol{k})} + \{\boldsymbol{w}_s(\boldsymbol{k})\times\boldsymbol{B}\}\cdot\nabla_{\boldsymbol{k}}\,\delta f_s(\boldsymbol{k})\right] = I_{\rm coll}[f_s(\boldsymbol{k})]\,. \tag{21}$$

For the sake of definiteness, we choose the set-up comprising $\boldsymbol{B} = B\,\hat{\boldsymbol{z}}$ and $\boldsymbol{E} = E\,\hat{\boldsymbol{z}}$. We parametrise the deviation in the particles' distribution-functions as

$$\delta f_s(\boldsymbol{k}) = -\,e\,\frac{\partial f_0(\xi_s)}{\partial\xi_s}\,\boldsymbol{E}\cdot\boldsymbol{\Lambda}_s(\boldsymbol{k}) = -\,e\,\frac{\partial f_0(\xi_s(\boldsymbol{k}))}{\partial\xi_s(\boldsymbol{k})}\,E\,\Lambda^z_s(\boldsymbol{k})\,, \tag{22}$$

where $\mathbf{\Lambda}_s(\boldsymbol{k})$ is the vectorial mean-free path. Because of our specific choice of coordinates, only the z-component of $\mathbf{\Lambda}_s(\boldsymbol{k})$ [i.e., $\Lambda^z_s(\boldsymbol{k})$] emerges as the nontrivial component as a result of the probe electric field. Consequently, the only equation that needs to be solved turns out to be

$$w^z_s(\boldsymbol{k}) + e\,B\,[\mathbf{\Omega}_s(\boldsymbol{k})\cdot\boldsymbol{w}_s(\boldsymbol{k})] - \,e\,B\,[\boldsymbol{w}_s(\boldsymbol{k})\times\hat{\boldsymbol{z}}(\boldsymbol{k})]\cdot\nabla_{\boldsymbol{k}}\Lambda^z_s(\boldsymbol{k}) = \mathcal{D}^{-1}_s(\boldsymbol{k})\sum_{\tilde{\chi},\tilde{s}}\int_{k'}\mathcal{M}_{s,\tilde{s}}(\boldsymbol{k},\boldsymbol{k}')\left[\Lambda^z_{\tilde{s}}(\boldsymbol{k}') - \Lambda^z_s(\boldsymbol{k})\right]. \tag{23}$$

Looking at the structure of the terms on both the sides, we infer that $\Lambda^z_s \equiv \Lambda^z_s(\mu,\theta)$ at an energy μ. In other words,$\delta f_s(\boldsymbol{k})$ can depend only on the polar angle, θ, and the chemical potential, μ, because the integral over the full momentum space effective gets substitutes by an integral over the Fermi surface at energy $\xi_s(\boldsymbol{k}) = \mu$. Essentially, the dependence on the azimuthal angle ϕ drops out because of the residual rotational symmetry of the system about the z-axis. This makes the momentum-space integrals reduce to the respective Fermi surfaces, $\xi_s(k^s_F,\theta) = \mu$, with the θ-dependent radii of $\{k^s_F(\theta)\}$ (parametrising the local Fermi momenta). Overall, the justification of assuming the ϕ-independent forms of $\{\Lambda^z_s \equiv \Lambda^z_s(\mu,\theta)\}$ is evident from the self-consistency — $[\mathbf{\Omega}_s(\boldsymbol{k})\cdot\boldsymbol{w}_s(\boldsymbol{k})]$ is ϕ-independent and $[\boldsymbol{w}_s(\boldsymbol{k})\times\hat{\boldsymbol{z}}]\cdot\nabla_{\boldsymbol{k}}\Lambda^z_s(\mu,\theta)$ reduces to zero.

Making use of the above arguments, we can now compute the spinor overlaps, $\left|\{\psi_{\tilde{s}}(\boldsymbol{k}')\}^\dagger\,\psi_s(\boldsymbol{k})\right|^2$, with the help of Eq. (6). Knowing that the dependence of the azimuthal angles, ϕ and ϕ', will disappear once we perform the azimuthal-angle integrations, we list the overlap-functions as

$$\begin{aligned}\mathcal{T}_{s,\tilde{s}}(\theta,\theta') = &\left[5 - 3\cos^2\theta' + \cos\theta\left(17\cos\theta' - 27\cos^3\theta'\right) + \cos^2\theta\left(9\cos^2\theta' - 3\right) + 9\cos^3\theta\cos\theta'\left(5\cos^2\theta' - 3\right)\right]\beta^{1,1}_{\text{intra}}\\ &+ \left[5 - 3\cos^2\theta' + \cos\theta\left(9\cos\theta' - 3\cos^3\theta'\right) + \cos^2\theta\left(9\cos^2\theta' - 3\right) + \cos^3\theta\left(5\cos^3\theta' - 3\cos\theta'\right)\right]\beta^{3,3}_{\text{intra}}\\ &+ \left[3 + 3\cos^2\theta' + \cos^3\theta\left(9\cos\theta' - 15\cos^3\theta'\right) + \cos\theta\left(9\cos^3\theta' - 3\cos\theta'\right) + \cos^2\theta\left(3 - 9\cos^2\theta'\right)\right]\beta_{\text{inter}}\,.\end{aligned} \tag{24}$$

Here, the answer contains the results obtained after already performing the trivial ϕ-integrals. We are now ready to solve Eq. (23), starting from its simplified version of

$$h_s(\mu,\theta) = \sum_{\tilde{s}} V\int_{k'}\mathcal{M}_{s,\tilde{s}}(\boldsymbol{k},\boldsymbol{k}')\,\Lambda^z_{\tilde{s}}(\mu,\theta') - \frac{\Lambda^z_s(\mu,\theta)}{\tau_s(\mu,\theta)}\,, \tag{25}$$

where

$$\tau^{-1}_s(\mu,\theta) = \sum_{\tilde{s}} V\int_{k'}\mathcal{M}_{s,\tilde{s}}(\boldsymbol{k},\boldsymbol{k}')\,, \quad h_s(\mu,\theta) = \mathcal{D}_s(\boldsymbol{k})\left[w^z_s(\boldsymbol{k}) + e\,B\,\{\mathbf{\Omega}_s(\boldsymbol{k})\cdot\boldsymbol{w}_s(\boldsymbol{k})\}\right]. \tag{26}$$

Incorporating the energy-conservation restrictions, which reduce the integrals to the respective Fermi surfaces at energy μ, we simply it even further to

$$h_s(\mu,\theta) + \frac{\Lambda^z_s(\mu,\theta)}{\tau_s(\mu,\theta)} = \sum_{\tilde{s}}\frac{\rho_{\text{imp}}\left|\mathcal{V}_{s,\tilde{s}}\right|^2}{16\times 4\,\pi}\int d\theta'\,\frac{\sin\theta'(k')^3\,\mathcal{D}^{-1}_{\tilde{s}}(\boldsymbol{k}')}{|\boldsymbol{k}'\cdot\boldsymbol{w}_s(\boldsymbol{k}')|}\,\mathcal{T}_{s,\tilde{s}}(\theta,\theta')\,\Lambda^z_{\tilde{s}}(\mu,\theta')\Big|_{k'=k^{\tilde{s}}_F}. \tag{27}$$

We note that the factor $(k')^3\sin\theta'$ arises as the Jacobian for switching to the spherical polar coordinates. Tacking the initial factor of $\delta\Big(\xi_{\tilde{s}}(\boldsymbol{k}') - \mu\Big)$ needs re-expressing it in the language of $\delta(k' - k^{\tilde{s}}_F)$, which sources the appearance of the other multiplicative factor of

$$\left|\hat{\boldsymbol{k}}'\cdot\nabla_{\boldsymbol{k}'}\xi_s(\boldsymbol{k}')\right|^{-1} = k'/|\boldsymbol{k}'\cdot\boldsymbol{w}_s(\boldsymbol{k}')|\,.$$

As a final step, observing the powers of $\cos\theta$ in (24)], we set forth an ansatz of

$$\Lambda^z_s(\mu,\theta) = \tau_s(\mu,\theta)\left[\lambda_s - h_s + a_s\cos\theta + b_s\cos^2\theta + c_s\cos^3\theta\right]. \tag{28}$$

In total we have 8 undetermined coefficients so determine, denoted as the set $\{\lambda_s,\, a_s,\, b_s,\, c_s\}$. We have 8 linear equations at our disposal, extracted from Eq. (27) by equating the coefficients of 1, $\cos\theta$, $\cos^2\theta$, and $\cos^3\theta$ on both the sides for each value of s. This system of linear equations can be expressed compactly as a matrix equation, captured by

$$\mathcal{A}\mathcal{N} = \Upsilon\,,\ \text{where}\ \mathcal{N} = \begin{bmatrix}\lambda_{1/2} & a_{1/2} & b_{1/2} & c_{1/2} & \lambda_{3/2} & a_{3/2} & b_{3/2} & c_{3/2}\end{bmatrix}^{\mathrm{T}}. \tag{29}$$

But there is a catch: the eight equations represented above are not linearly independent. This is because $\mathcal{A}$'s rank is lower than 8. It is actually well and good since it prevents from the system from becoming overdetermined, as we must also employ the constraint of the electron-number conservation, embodied by

$$\sum_s \int_k \delta f_s(\boldsymbol{k}) = 0\,. \tag{30}$$

Plugging in the solutions obtained, the charge-current density along the z-direction is computed as

$$J_z^{\mathrm{tot}} = -\,\frac{e}{V}\sum_s \int_k (\dot{\boldsymbol{r}}\cdot\hat{\boldsymbol{z}})\;\delta f_s(\boldsymbol{k})\,, \tag{31}$$

finally leading to the desired longitudinal magnetoconductivity,

$$\sigma_{zz}^{\mathrm{tot}} = \sum_s \sigma_{zz}^s\,,\quad \sigma_{zz}^s = -\,\frac{e^2}{V}\int \frac{d^3\boldsymbol{k}}{(2\,\pi)^3}\,[w_s^z(\boldsymbol{k}) + e\,B\,\{\boldsymbol{\Omega}_s(\boldsymbol{k})\cdot\boldsymbol{w}_s(\boldsymbol{k})\}]\,\delta\big(\xi_s(\boldsymbol{k}) - \mu\big)\,\Lambda_s^z(\mu,\theta)\,. \tag{32}$$

doi.org/10.32388/NoMLRZ

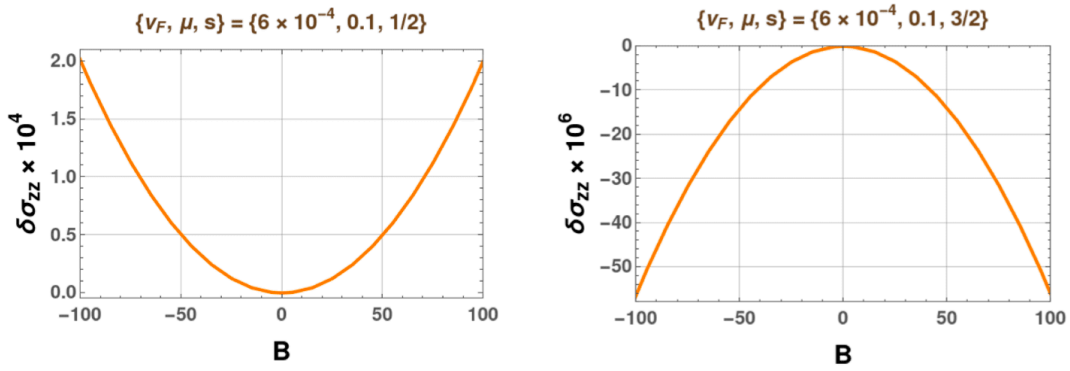

(a)

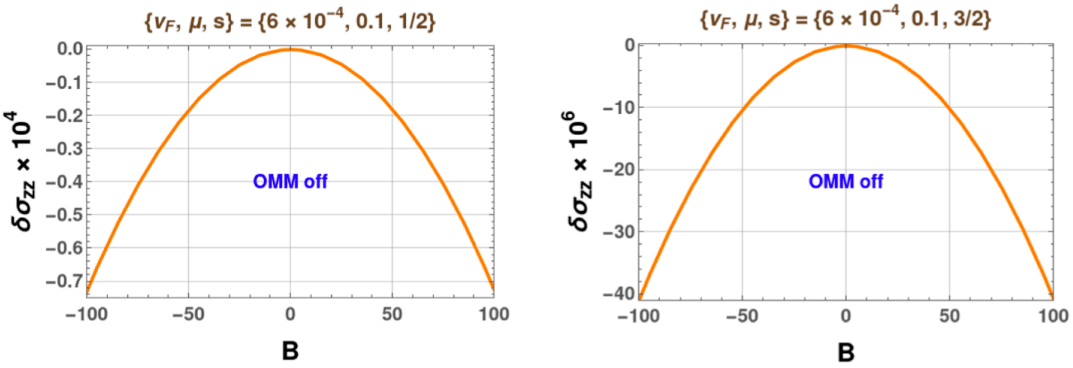

(b)

Figure 2. $\delta\sigma_{zz}(s)$ from each of the bands considering no interband interactions, with $\beta^{s,s}_{\text{intra}}$ set to unity: While subfigure (a) depicts the variation of the full conductivity with B (in eV^2) when OMM is taken into account appropriately, subfigure (b) represents the conductivity versus B characteristics when OMM is turned off. Here, μ is in eV.

C. Results and discussions

The solutions of Eq. (27) are obtained numerically for a given set of parameter-values. In our illustrations, we resort to plotting

$$\delta\sigma_{zz}(s) \equiv \sigma^s_{zz}(B)/\sigma^s_{zz}(B=0) - 1,$$

where the residual conductivity at $B = 0$ (i.e., the Drude part) is subtracted off. The parameter values have been taken from Ref. [58]. There, $\hbar v_F = 1.23$ eV Å, which translates into

$$v_F = \frac{1.23 \times 10^{-10}\ \text{m eV}}{6.58 \times 10^{-16}\ \text{eV s}} = 0.1869 \times 10^6\ \text{m/s} \simeq 0.06 \times 10^{-2}\, c\,,$$

where c is the speed of light. Therefore, in natural units, we set the value of v_F to 6×10^{-4}.

To start with, we attempt to make sense of the response-characteristics for the scenarios when there is no interband scattering, i.e., β_{inter} is set to zero. This leads to the reduction of $\mathcal{A}$ into the direct sum of the two matrices, $\mathcal{A}_1$ and $\mathcal{A}_2$, each of them being a 4×4 matrix. In every case, we find that they have rank 3 (instead of 4), with $\int_k \delta f_s(\boldsymbol{k}) = 0$ providing the necessary extra equation. Fig. 2 captures such a scenario. Curiously, the parabolic-shaped response-profiles curve in opposite ways for

doi.org/10.32388/NoMLRZ

$s = 1/2$ and $s = 3/2$. In order to gauge the nature of the OMM-contributions, the lower panel represent the behaviour bbtained by switching off the OMM. It leads to the conclusion that (I) the OMM-parts come with a positive sign and are strong enough to flip the BC-only response into the positive domain for $s = 1/2$; (II) the OMM-contributions have a negative sign which assist in increasing the magnitude of the already negative-valued response (from the BC-only parts) for $s = 3/2$.

Fig. 3 shows the generic situations when the quasiparticles populating both the bands can scatter with each other. The 8×8 matrix $\mathcal{A}$ is found to have rank 7, ensuring the internal consistency of the available equations. As discussed earlier, this means that the charge-conservation provides the remaining linearly independent equation [viz., Eq. (30)]. From the data presented here as well as our scans of the parameter space (not shown here), we find that for $\beta_{\rm inter}/\beta^{s,s}_{\rm intra}$ greater than some small threshold value, the curves for $s = 3/2$ are turned upside down (into the negative domain), while the $s = 1/2$ continuing to curve upwards (remaining positive). To probe into the role of the OMM-sourced parts, we plot the nature of the curves by switching off the OMM (lower panel of Fig. 3). Intriguingly, the curves for $s = 1/2$ and $s = 3/2$ behave in an opposite nature, the former always remaining negatve and curving downward, irrespective of the values of $\beta_{\rm inter}$. Overall, comparing the upper and the lower panels, we conclude that, while the OMM-parts have a positive sign and are strong enough to flip the BC-only response into the positive domain for $s = 1/2$, the OMM-contributions have a negative sign and try to pull the positive-valued response (from the BC-only parts) towards lower values for $s = 3/2$

Overall, $\sigma^s_{zz}(B)$ comprises only even powers of B, which is in agreement with the Onsager-Casimir reciprocity relation, $\sigma^{\rm intra(inter)}_{zz}(\mathbf{B}) = \sigma^{\rm intra(inter)}_{zz}(-\mathbf{B})$[64][65][66]. From analysing the generic features, we conclude that there is little wisdom to be gained from the $\beta_{\rm inter} = 0$ to infer anything regarding the $\beta_{\rm inter} \neq 0$ case. The only thing that matches between the two separate analyses is regarding the signs and strengths of the OMM-sourced parts. Albeit, the rationale behind not to try to extract similarities between the two cases is that the charge conservation equation(s) that come into picture are distinctly different — (I) for a single band with $\beta_{\rm inter} = 0$, the charge conservation must be satisfied individually for that particular band; (II) a nonzero interband-coupling demands that the net charge, from summing over the two bands, must be conserved. The observations serve to reinforce the recurrent phenomenon that the response from a single isolated band is fundamentally different from the case when the quasiparticles are free to scatter with those populating other bands. In fact, the same thing has been onserved for the two bands of an isolated Kramers-Weyl node[35], where downward-curved parabolas morph into upward-curved ones for each of the bands, as soon as $\beta_{\rm inter}$ is turned on.

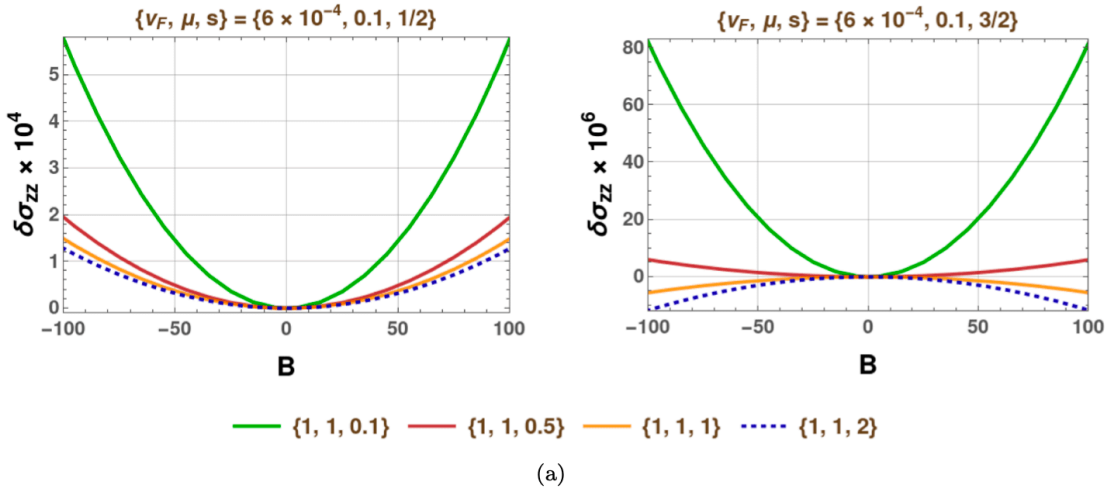

(a)

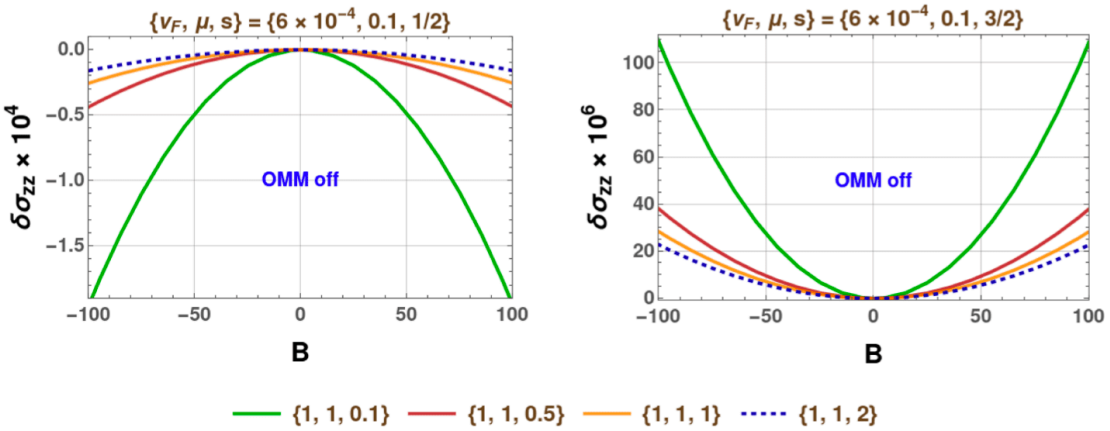

(b)

Figure 3. $\delta\sigma_{zz}(s)$ from each of the bands considering both intraband and interband interactions. While subfigure (a) depicts the variation of the full conductivity with respect to B (in eV^2) when OMM is taken into account appropriately, subfigure (b) represents the conductivity-versus-B profiles when OMM is switched off. The three numbers in each plot-legend indicate the values in the set $\{\beta_{\rm intra}^{1/2,1/2}, \beta_{\rm intra}^{3/2,3/2}, \beta_{\rm inter}\}$. Here, μ is in eV.

IV. Summary and outlook

In the current piece of work, we have ventured into determining the nature of the linear response in the form of longitudinal magnetoconductivity, focussing on on isolated RSWN. We have attempted to include both the BC and the OMM in a cohesive manner, as the necessary topological ingredients in the semiclassical Boltzmann equations. A major stride forward has been to solve the linearised (in the strength of the probe field) equations exactly, not limiting to the relaxation-time approximation with a constant phenomenological time (τ). Needless to say, our results quantify the serious drawbacks of using momentum-independent relaxation times and neglecting the angle-dependent spinor-overlaps in the collision integrals (see Refs. [33][34] for the analytical expressions). By comparing the nontrivial results with those obtained in our earlier works [33][34], we do identify the inadequacies of dropping the angular-dependence in τ and the ramifications of the nontrivial spinor-structures, as the exact

answers turn out to be fundamentally different. Of course, in Ref. [33], we did not account for interband scatterings, and neither shall we attempt to do so anymore, because we have already successfully implemented the generic formalism without resorting to any approximation. Another point is that, a linear-in-momentum term accompanying the identity matrix (in the operator space for the four-component spinors), is not allowed in the most generic Hamiltonian for the RSWNs [58] derived from group-theoretical arguments. Consequently, tilting is completely irrelevant for the RSWNs, preventing the possibility of having odd powers of B. We note that tilting is a ubiquitous feature of the WSMs[9][11][13][67][68], because the conventional Weyl nodes generically appear at the low-symmetry points of the BZs (not limited to those of chiral crystals).

In the future, it will be a rewarding enterprise to redo the calculations of linear response at finite temperatures[8][9][11][15][16][33][63][69], which will also enable us to compute the temperature-dependent linear-response coefficients like the thermoelectric and thermal-conductivity tensors. Another avenue worth exploring is to investigate the effects of strain[8][11][33][70], which breaks the rotational symmetry and can lead to pseudomagnetic fields ($\boldsymbol{B}_5$). A nonzero $\boldsymbol{B}_5$ makes it possible for odd powers of B to show up in the response.

References

1. ^Burkov AA, Balents L (2011). "Weyl semimetal in a topological insulator multilayer." Phys Rev Lett. **107**:127205. doi:10.1103/physrevlett.107.127205.
2. ^Armitage NP, Mele EJ, Vishwanath A (2018). "Weyl and Dirac semimetals in three-dimensional solids." Rev Mod Phys. **90**(1):015001. doi:10.1103/revmodphys.90.015001.
3. ^Yan B, Felser C (2017). "Topological Materials: Weyl Semimetals." Annual Review of Condensed Matter Physics. **8**(1):337–354. doi:10.1146/annurev-conmatphys-031016-025458.
4. ^Berry MV (1984). "Quantal phase factors accompanying adiabatic changes." Proceedings of the Royal Society of London. A. Mathematical and Physical Sciences. **392**(1802):45–57. doi:10.1098/rspa.1984.0023.
5. a, bXiao D, Chang MC, Niu Q (2010). "Berry phase effects on electronic properties." Rev Mod Phys. **82**(3):1959–2007. doi:10.1103/revmodphys.82.1959.
6. a, b, c, dSundaram G, Niu Q (1999). "Wave-packet dynamics in slowly perturbed crystals: Gradient corrections and Berry-phase effects." Phys Rev B. **59**(23):14915–14925. doi:10.1103/physrevb.59.14915.
7. ^Graf A, Piéchon F (2021). "Berry curvature and quantum metric in N-band systems: An eigenprojector approach." Phys Rev B. **104**(8):085114. doi:10.1103/physrevb.104.085114.
8. a, b, cGhosh R, Mandal I (2024). "Electric and thermoelectric response for Weyl and multi-Weyl semimetals in planar Hall configurations including the effects of strain." Physica E: Low-dimensional Systems and Nanostructures. **159**:115914. doi:10.1016/j.physe.2024.115914.
9. a, b, cGhosh R, Mandal I (2024). "Direction-dependent conductivity in planar Hall set-ups with tilted Weyl/multi-Weyl semimetals." Journal of Physics: Condensed Matter. **36**(27):275501. doi:10.1088/1361-648x/ad38fa.
10. ^Balduini F, Molinari A, Rocchino L, Hasse V, Felser C, Sousa M, Zota C, Schmid H, Grushin AG, Gotsmann B (2024). "Intrinsic negative magnetoresistance from the chiral anomaly of multifold fermions." Nature Communications. **15**(1):6526. doi:10.1038/s41467-024-50451-5.

11. ^ a b c d Medel L, Ghosh R, Martín-Ruiz A, Mandal I (2024). "Electric, thermal, and thermoelectric magnetoconductivity for Weyl/multi-Weyl semimetals in planar Hall set-ups induced by the combined effects of topology and strain." Scientific Reports. **14**(1):21390. doi:10.1038/s41598-024-68615-0.
12. ^ a b c Knoll A, Timm C, Meng T (2020). "Negative longitudinal magnetoconductance at weak fields in Weyl semimetals." Phys Rev B. **101**(20):201402. doi:10.1103/physrevb.101.201402.
13. ^ a b Mandal I (2024). "Anisotropic conductivity for the type-I and type-II phases of Weyl/multi-Weyl semimetals in planar Hall set-ups." arXiv e-prints. https://ui.adsabs.harvard.edu/abs/2024arXiv241005028M.
14. ^ a b Li Y, Wang Z, Li P, Yang X, Shen Z, Sheng F, Li X, Lu Y, Zheng Y, Xu ZA (2017). "Negative magnetoresistance in Weyl semimetals NbAs and NbP: Intrinsic chiral anomaly and extrinsic effects." Frontiers of Physics. **12**(3):127205. doi:10.1007/s11467-016-0636-8.
15. ^ a b c d e f Mandal I, Saha S, Ghosh R (2025). "Signatures of topology in generic transport measurements for Rarita-Schwinger-Weyl semimetals." Solid State Communications. **397**:115799. doi:10.1016/j.ssc.2024.115799.
16. ^ a b Haidar F, Mandal I (2025). "Reflections of topological properties in the planar-Hall response for semimetals carrying pseudospin-1 quantum numbers." Annals of Physics. **478**:170010. doi:10.1016/j.aop.2025.170010.
17. ^ a b c d Mandal I (2025). "Longitudinal magnetoconductivity in chiral multifold semimetals exemplified by pseudospin-1 nodal points." arXiv e-prints. https://arxiv.org/abs/2505.19636.
18. ^ Rather FH, Jaffar AM, Mandal I (2025). "Direction-dependent linear response for gapped nodal-line semimetals in planar-Hall configurations." arXiv e-prints. https://ui.adsabs.harvard.edu/abs/2025arXiv250310712H.
19. ^ a b c Bradlyn B, Cano J, Wang Z, Vergniory MG, Felser C, et al. (2016). "Beyond Dirac and Weyl fermions: Unconventional quasiparticles in conventional crystals." Science. **353**(6299). https://science.sciencemag.org/content/353/6299/aaf5037.
20. ^ Liang L, Yu Y (2016). "Semimetal with both Rarita-Schwinger-Weyl and Weyl excitations." Phys Rev B. **93**(4):045113. doi:10.1103/physrevb.93.045113.
21. ^ Boettcher I (2020). "Interplay of Topology and Electron-Electron Interactions in Rarita-Schwinger-Weyl semimetals." Phys Rev Lett. **124**(12):127602. doi:10.1103/physrevlett.124.127602.
22. ^ Link JM, Boettcher I, Herbut IF (2020). "d-wave superconductivity and Bogoliubov-Fermi surfaces in Rarita-Schwinger-Weyl semimetals." Phys Rev B. **101**(18):184503. doi:10.1103/physrevb.101.184503.
23. ^ Isobe H, Fu L (2016). "Quantum critical points of j=3/2 Dirac electrons in antiperovskite topological crystalline insulators." Phys Rev B. **93**(24):241113. doi:10.1103/physrevb.93.241113.
24. ^ a b Tang P, Zhou Q, Zhang SC (2017). "Multiple Types of Topological Fermions in Transition Metal Silicides." Phys Rev Lett. **119**(20):206402. doi:10.1103/physrevlett.119.206402.
25. ^ Mandal I (2020). "Transmission in pseudospin-1 and pseudospin-3/2 semimetals with linear dispersion through scalar and vector potential barriers." Physics Letters A. **384**(27):126666. doi:10.1016/j.physleta.2020.126666.
26. ^ a b c Sekh S, Mandal I (2022). "Circular dichroism as a probe for topology in three-dimensional semimetals." Phys Rev B. **105**(23):235403. doi:10.1103/physrevb.105.235403.
27. ^ Ma JZ, Wu QS, Song M, Zhang SN, Guedes EB, Ekahana SA, Krivenkov M, Yao MY, Gao SY, Fan WH, Qian T, Ding H, Plumb NC, Radovic M, Dil JH, Xiong YM, Manna K, Felser C, Yazyev OV, Shi M (2021). "Observation of a singular Weyl point surrounded by charged nodal walls in PtGa." Nature Communications. **12**(1):3994. doi:10.1038/s41467-021-24289-0.

28. ^ a b Sekh S, Mandal I (2022). "Magnus Hall effect in three-dimensional topological semimetals." Eur Phys J Plus. **137**(6):736. doi:10.1140/epjp/s13360-022-02840-2.
29. ^ a b Mandal I (2023). "Transmission and conductance across junctions of isotropic and anisotropic three-dimensional semimetals." European Physical Journal Plus. **138**(11):1039. doi:10.1140/epjp/s13360-023-04652-4.
30. ^ a b Mandal I (2024). "Andreev bound states in superconductor-barrier-superconductor junctions of Rarita-Schwinger-Weyl semimetals." Physics Letters A. **503**:129410. doi:10.1016/j.physleta.2024.129410.
31. ^ a b c Chang G, Wieder BJ, Schindler F, Sanchez DS, Belopolski I, Huang SM, Singh B, Wu D, Chang TR, Neupert T, Xu SY, Lin H, Hasan MZ (2018). "Topological quantum properties of chiral crystals." Nature Materials. **17**(11):978–985. doi:10.1038/s41563-018-0169-3.
32. ^ Flicker F, de Juan F, Bradlyn B, Morimoto T, Vergniory MG, Grushin AG (2018). "Chiral optical response of multifold fermions." Phys Rev B. **98**(15):155145. doi:10.1103/physrevb.98.155145.
33. ^ a b c d e f g h i j k l m Ghosh R, Haidar F, Mandal I (2024). "Linear response in planar Hall and thermal Hall setups for Rarita-Schwinger-Weyl semimetals." Phys Rev B. **110**(24):245113. doi:10.1103/physrevb.110.245113.
34. ^ a b c d e f g Mandal I (2025). "Chiral anomaly and internode scatterings in multifold semimetals." Phys Rev B. **111**(16):165116. doi:10.1103/physrevb.111.165116.
35. ^ a b c d Mandal I (2025). "Disentangling contributions to longitudinal magnetoconductivity for Kramers-Weyl nodes." arXiv e-prints. https://arxiv.org/abs/2506.07913.
36. ^ Cayssol J, Fuchs JN (2021). "Topological and geometrical aspects of band theory." Journal of Physics: Materials. **4**(3):034007. doi:10.1088/2515-7639/abf0b5.
37. ^ Polash MMH, Yalameha S, Zhou H, Ahadi K, Nourbakhsh Z, Vashaee D (2021). "Topological quantum matter to topological phase conversion: Fundamentals, materials, physical systems for phase conversions, and device applications." Materials Science and Engineering: R: Reports. **145**:100620. doi:10.1016/j.mser.2021.100620.
38. ^ Nielsen HB, Ninomiya M (1981). "A no-go theorem for regularizing chiral fermions." Physics Letters B. **105**(2):219–223. doi:10.1016/0370-2693(81)91026-1.
39. ^ Lv BQ, Weng HM, Fu BB, Wang XP, Miao H, Ma J, Richard P, Huang XC, Zhao LX, Chen GF, Fang Z, Dai X, Qian T, Ding H (2015). "Experimental Discovery of Weyl Semimetal TaAs." Phys Rev X. **5**(3):031013. doi:10.1103/physrevx.5.031013.
40. ^ Nielsen HB, Ninomiya M (1983). "The Adler-Bell-Jackiw anomaly and Weyl fermions in a crystal." Physics Letters B. **130**(6):389–396. doi:10.1016/0370-2693(83)91529-0.
41. ^ Son DT, Spivak BZ (2013). "Chiral anomaly and classical negative magnetoresistance of Weyl metals." Phys Rev B. **88**(10):104412. doi:10.1103/physrevb.88.104412.
42. ^ He WY, Xu XY, Law KT (2021). "Kramers Weyl semimetals as quantum solenoids and their applications in spin-orbit torque devices." Communications Physics. **4**(1):66. doi:10.1038/s42005-021-00564-w.
43. ^ a b c Chang G, Xu SY, Wieder BJ, Sanchez DS, Huang SM, Belopolski I, Chang TR, Zhang S, Bansil A, Lin H, Hasan MZ (2017). "Unconventional Chiral Fermions and Large Topological Fermi Arcs in RhSi." Phys Rev Lett. **119**(20):206401. doi:10.1103/physrevlett.119.206401.
44. ^ Ni Z, Wang K, Zhang Y, Pozo O, Xu B, Han X, Manna K, Paglione J, Felser C, Grushin AG, de Juan F, Mele EJ, Wu L (2021). "Giant topological longitudinal circular photo-galvanic effect in the chiral multifold semimetal CoSi." Nature Communications. **12**(1):154. doi:10.1038/s41467-020-20408-5.

45. ^Moore JE (2018). "Optical properties of Weyl semimetals." National Science Review. **6**(2):206–208. doi:10.1093/nsr/nwy164.

46. ^Guo C, Asadchy VS, Zhao B, Fan S (2023). "Light control with Weyl semimetals." eLight. **3**(1):2. doi:10.1186/s43593-022-00036-w.

47. ^Avdoshkin A, Kozii V, Moore JE (2020). "Interactions Remove the Quantization of the Chiral Photocurrent at Weyl Points." Phys Rev Lett. **124**(19):196603. doi:10.1103/physrevlett.124.196603.

48. ^Mandal I (2020). "Effect of interactions on the quantization of the chiral photocurrent for double-Weyl semimetals." Symmetry. **12**(6). https://www.mdpi.com/2073-8994/12/6/919.

49. ^Mandal I (2024). "Signatures of two- and three-dimensional semimetals from circular dichroism." International Journal of Modern Physics B. **38**(17):2450216. doi:10.1142/S0217979224502163.

50. ^Hasan MZ, Chang G, Belopolski I, Bian G, Xu SY, et al. (2021). "Weyl, Dirac and high-fold chiral fermions in topological quantum materials." arXiv e-prints. arXiv:2103.01714. doi:10.48550/arXiv.2103.01714.

51. ^Zhang CL, Schindler F, Liu H, Chang TR, Xu SY, Chang G, Hua W, Jiang H, Yuan Z, Sun J, Jeng HT, Lu HZ, Lin H, Hasan MZ, Xie XC, Neupert T, Jia S (2017). "Ultraquantum magnetoresistance in the Kramers-Weyl semimetal candidate β-Ag2Se." Phys Rev B. **96**(16):165148. doi:10.1103/physrevb.96.165148.

52. a, b, cSanchez DS, Belopolski I, Cochran TA, Xu X, Yin JX, Chang G, Xie W, Manna K, Süss V, Huang CY, Alidoust N, Multer D, Zhang SS, Shumiya N, Wang X, Wang GQ, Chang TR, Felser C, Xu SY, Jia S, Lin H, Hasan MZ (2019). "Topological chiral crystals with helicoid-arc quantum states." Nature. **567**(7749):500–505. doi:10.1038/s41586-019-1037-2.

53. ^Schröter NBM, Pei D, Vergniory MG, Sun Y, Manna K, de Juan F, Krieger JA, Süss V, Schmidt M, Dudin P, Bradlyn B, Kim TK, Schmitt T, Cacho C, Felser C, Strocov VN, Chen Y (2019). "Chiral topological semimetal with multifold band crossings and long Fermi arcs." Nature Physics. **15**(8):759–765. doi:10.1038/s41567-019-0511-y.

54. ^Mardanya S, Kargarian M, Verma R, Chang TR, Chowdhury S, Lin H, Bansil A, Agarwal A, Singh B (2024). "Unconventional superconducting pairing in a B20 multifold Weyl fermion semimetal." Phys Rev Mater. **8**(9):L091801. doi:10.1103/physrevmaterials.8.l091801.

55. a, bGao ZS, Gao XJ, He WY, Xu XY, Ng TK, Law KT (2022). "Topological superconductivity in multifold fermion metals." Quantum Frontiers. **1**(1):3. doi:10.1007/s44214-022-00001-1.

56. a, b, c, dAshcroft NW, Mermin ND (2011). Solid state physics. Cengage Learning. https://books.google.de/books?id=x_s_YAAACAAJ. ISBN 9788131500521.

57. a, b, c, dMandal I, Saha K (2024). "Thermoelectric Response in Nodal-Point Semimetals." Ann Phys (Berlin). **536**(9):2400016. doi:10.1002/andp.202400016.

58. a, b, cXu B, Fang Z, Sánchez-Martínez MA, Venderbos JWF, Ni Z, Qiu T, Manna K, Wang K, Paglione J, Bernhard C, Felser C, Mele EJ, Grushin AG, Rappe AM, Wu L (2020). "Optical signatures of multifold fermions in the chiral topological semimetal CoSi." Proceedings of the National Academy of Sciences. **117**(44):27104–27110. doi:10.1073/pnas.2010752117.

59. ^Xiao D, Yao W, Niu Q (2007). "Valley-Contrasting Physics in Graphene: Magnetic Moment and Topological Transport." Phys Rev Lett. **99**(23):236809. doi:10.1103/physrevlett.99.236809.

60. ^Graf A (2022). Aspects of multiband systems: Quantum geometry, flat bands, and multifold fermions. Theses, Université Paris-Saclay. https://theses.hal.science/tel-04047054.

61. a, b, cLi L, Cao J, Cui C, Yu ZM, Yao Y (2023). "Planar hall effect in topological Weyl and nodal-line semimetals." Phys Rev B. **108**(8):085120. doi:10.1103/physrevb.108.085120.

62. ^Mandal I, Saha K (2020). "Thermopower in an anisotropic two-dimensional Weyl semimetal." Phys Rev B. **101**(4):045101. doi:10.1103/physrevb.101.045101.

63. a, bMandal I (2025). "Linear response of tilted anisotropic two-dimensional Dirac cones." The European Physical Journal B. **98**(6):123. doi:10.1140/epjb/s10051-025-00945-y.

64. ^Onsager L (1931). "Reciprocal Relations in Irreversible Processes. I." Phys Rev. **37**(4):405–426. doi:10.1103/PhysRev.37.405.

65. ^Casimir HBG (1945). "On Onsager's principle of microscopic reversibility." Rev Mod Phys. **17**(2-3):343–350. doi:10.1103/RevModPhys.17.343.

66. ^Jacquod P, Whitney RS, Meair J, Büttiker M (2012). "Onsager relations in coupled electric, thermoelectric, and spin transport: The ten fold way." Phys Rev B. **86**(15):155118. doi:10.1103/PhysRevB.86.155118.

67. ^Stålhammar M, Larana-Aragon J, Knolle J, Bergholtz EJ (2020). "Magneto-optical conductivity in generic Weyl semimetals." Phys Rev B. **102**(23):235134. doi:10.1103/PhysRevB.102.235134.

68. ^Yadav S, Sekh S, Mandal I (2023). "Magneto-optical conductivity in the type-I and type-II phases of Weyl/multi-Weyl semimetals." Physica B: Condensed Matter. **656**:414765. doi:10.1016/j.physb.2023.414765.

69. ^Mandal I, Freire H (2024). "Transport properties in non-Fermi liquid phases of nodal-point semimetals." Journal of Physics: Condensed Matter. **36**(44):443002. doi:10.1088/1361-648x/ad665e.

70. ^Bose A, Narayan A (2021). "Strain-induced topological charge control in multifold fermion systems." Journal of Physics: Condensed Matter. **33**(37):375002. doi:10.1088/1361-648x/ac0fa0.

Declarations

Funding: No specific funding was received for this work.

Potential competing interests: No potential competing interests to declare.